

Long-Period Giant Companions to Three Compact, Multiplanet Systems

SEAN M. MILLS,¹ ANDREW W. HOWARD,¹ LAUREN M. WEISS,^{2,3} JASON H. STEFFEN,⁴ HOWARD ISAACSON,⁵
BENJAMIN J. FULTON,^{1,6} ERIK A. PETIGURA,¹ MOLLY R. KOSIAREK,^{7,8} LEA A. HIRSCH,^{5,9} AND JOHN H. BOISVERT⁴

¹*California Institute of Technology, Department of Astronomy
1200 East California Blvd, Pasadena, CA 91125, USA*

²*Institute for Astronomy, University of Hawaii
2680 Woodlawn Drive, Honolulu, HI 96822, USA*

³*Parrent Fellow*

⁴*University of Nevada, Las Vegas, Department of Physics and Astronomy
4505 S Maryland Pkwy, Las Vegas, NV 89155*

⁵*Department of Astronomy, University of California
510 Campbell Hall, Berkeley, CA 94720, USA*

⁶*IPAC-NASA Exoplanet Science Institute
Pasadena, CA 91125, USA*

⁷*Department of Astronomy and Astrophysics, University of California
Santa Cruz, CA 95064, USA*

⁸*NSF Graduate Research Fellow*

⁹*Kavli Institute for Particle Astrophysics and Cosmology
Stanford University, Stanford, CA 94305, USA*

ABSTRACT

Understanding the relationship between long-period giant planets and multiple smaller short-period planets is critical for formulating a complete picture of planet formation. This work characterizes three such systems. We present Kepler-65, a system with an eccentric ($e = 0.28 \pm 0.07$) giant planet companion discovered via radial velocities (RVs) exterior to a compact, multiply-transiting system of sub-Neptune planets. We also use precision RVs to improve mass and radius constraints on two other systems with similar architectures, Kepler-25 and Kepler-68. In Kepler-68 we propose a second exterior giant planet candidate. Finally, we consider the implications of these systems for planet formation models, particularly that the moderate eccentricity in Kepler-65’s exterior giant planet did not disrupt its inner system.

1. INTRODUCTION

Precise photometric monitoring of more than 100,000 stars over a four year period by the *Kepler* space mission (Borucki et al. 2010) has revealed thousands of planets and planetary candidates (Coughlin et al. 2016; Morton et al. 2016). Approximately half of these planets and candidates are found in systems of two or more transiting planets with orbital periods $\lesssim 1$ year. However, the existence of long-period or inclined planetary companions is rarely probed by the *Kepler* data alone (c.f., Nesvorný et al. 2012; Dawson et al. 2014). Therefore, we rely on radial velocity (RV) follow-up to probe the full architectures of planetary systems observed by *Kepler*.

Here we present results on three systems that have multiple transiting planets discovered by *Kepler* as well as long-period giant planet companions detected via RVs as part of the California Planet Search (CPS; Howard et al. 2010): Kepler-25, Kepler-65, and Kepler-68.

How giant planets exterior to super-Earths and sub-Neptunes (SEASNs) affect their formation and evolution is an open question in planetary science. It is speculated that Jupiter and Saturn prevented the typical short-period SEASNs observed in Kepler multiplanet systems from forming in the Solar System (Batygin & Laughlin 2015), with similar effects possible in exoplanet systems (Izidoro et al. 2015). This effect remains uncertain and in general it seems that the presence of warm and cool Jupiters does not prevent such compact SEASN architectures, and may even favor them (Zhu & Wu 2018; Bryan et al. 2018). Counterexamples include Kepler-90,

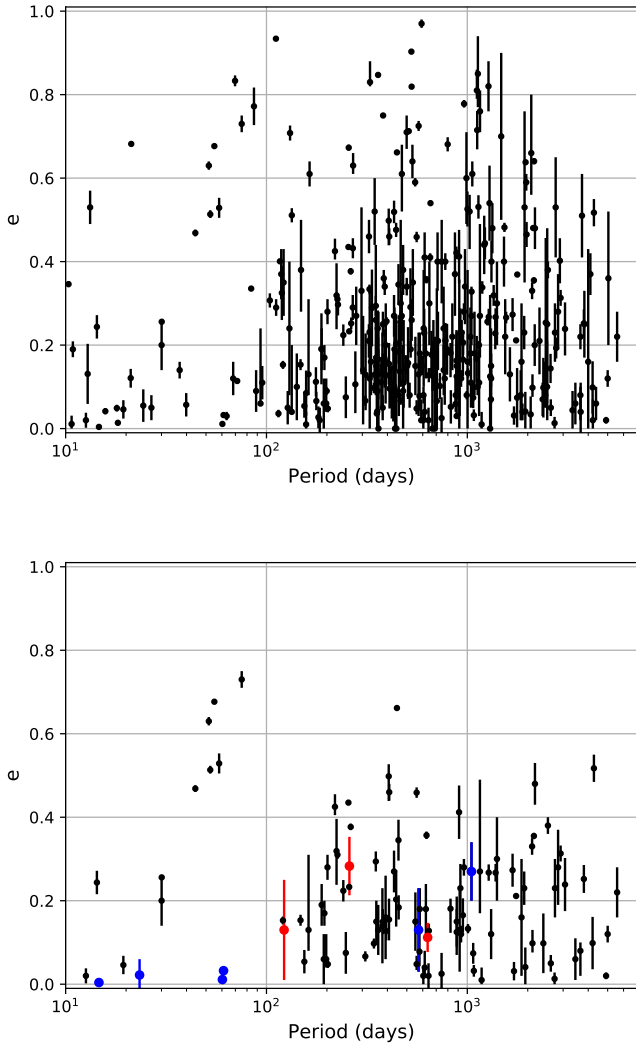


Figure 1. *Top:* The periods and eccentricities of warm and cool Jupiters: planets with $M \sin i > 0.5 M_{\text{Jupiter}}$ and $P > 10$ days that have eccentricity and eccentricity uncertainty data in the Exoplanet Orbit Database (<http://exoplanets.org>) as of October 2018 (Han et al. 2014). *Bottom:* The eccentricities of giant planets in multi-planet systems with measured eccentricities are shown in black. The majority are systems of planets with exactly two giant planets. Blue points highlight those planets with multiple small ($M < M_{\text{Saturn}}$ or $R < 8R_{\oplus}$) planets in the same system. The red points are a subset of those points which are the subject of this study.

a pair of coplanar, $e \approx 0$ giant planets exterior to 5 SEASNs (Cabrera et al. 2014) and WASP-47, a system with a $e \approx 0.27$, ~ 600 day Jupiter around a mixed system of 2 SEASNs and an $e \approx 0$ Jupiter at < 10 days – although the latter example may be atypical due to its relatively short-period Jupiter in addition to its exterior one (Becker et al. 2015; Sinukoff et al. 2017).

Warm and cool Jupiters (WCJs; $P \gtrsim 10$ days and $M \gtrsim 0.5 M_{\text{Jupiter}}$) have a very broad eccentricity distribution (Fig. 1). The mean eccentricities (\bar{e}) of these Jupiters is ≈ 0.3 , much higher than the Solar System planets ($\bar{e} \approx 0.06$) and Kepler multi-planet systems as measured via transit duration ratios (Rayleigh $\sigma_e \approx 0.03$; Fabrycky et al. 2014), using asteroseismology derived stellar densities ($\sigma_e \approx 0.05$; Van Eylen & Albrecht 2015), combining transit durations and spectroscopy ($\bar{e} \approx 0.04$; Xie et al. 2016), and via dynamical analyses ($\bar{e} \approx 0.02$; Hadden & Lithwick 2017). However, the WCJ e distribution is perhaps similar to systems with a single transiting warm super-Earth or sub-Neptune ($\bar{e} \sim 0.3$; Xie et al. 2016; Van Eylen et al. 2019).

While data are presently limited, it generally seems that systems with both multiple SEASNs and WCJs have dynamically cool Jupiters (e.g., Kepler-46, Kepler-148, Kepler-30, Kepler-89, Kepler-487, 55 Cnc, GJ 876, HD 34445, WASP-47, and Kepler-90)¹. Fig. 1 compares the distribution of measured giant planet eccentricities in different types of multiple planet systems. The low eccentricities of giants in planets with multiple SEASNs is intriguing compared to the general population of WCJs, both in single and multiple planet systems, where high eccentricities are common. Uehara et al. (2016) and Foreman-Mackey et al. (2016) also tentatively suggests that *Kepler* SEASN systems have coplanar (and thus dynamically cold) WCJ companions by showing evidence of potential > 2 -year period Jupiter companions². Even if WCJs are not barriers to planet formation, eccentric exterior Jupiters may excite any interior planets’ eccentricities and inclinations causing a reduction in either true planet multiplicity from ejections or observed multiplicity due to increased planet mutual inclinations (Huang et al. 2017; Pu & Lai 2018).

2. METHODS

In order to characterize the Kepler-25, Kepler-65, and Kepler-68 systems, we rely on a combination of the transit photometry, RVs, and precise stellar spectra. The photometric signals reveal the ratio of planetary to host star radii. With precise stellar properties derived from combining stellar spectra and parallax measurements (Fulton & Petigura 2018), the physical sizes of the planets can be determined. Additionally the planet-planet

¹ This list is incomplete as it only includes well-characterized Jupiters reported on exoplanets.org. For instance, Kepler-48, a long-period Jupiter around 3 SEASNs from Marcy et al. (2014), is not included.

² We note Uehara et al. (2016) also presents a few candidates of either eccentric long-period Jupiters or possibly Warm Jupiters based on transit duration, but this is uncertain.

gravitational interactions of closely spaced planets results in transit timing variations (TTVs) which reveal a combination of the mass and eccentricity of the planets (Agol et al. 2005; Lithwick et al. 2012). Modeling these TTVs can give mass constraints on the planets; however, with low signal-to-noise (S/N) data a mass-eccentricity degeneracy often remains (Lithwick et al. 2012; Deck & Agol 2015). These degeneracies can sometimes be broken by RV data that provide a complementary constraint (e.g., Petigura et al. 2018), or by a strong prior on eccentricity (Hadden & Lithwick 2017). We study Kepler-65 and Kepler-25 with a photodynamical model which produces synthetic RV and photometric data generated by the N-body interactions of simulated planets and compares it to the observed data to extract planetary orbital elements, masses, and radii self-consistently. Kepler-68 does not exhibit detectable TTVs because the planets are not closely-spaced or near resonance (Agol & Deck 2016; Holczer et al. 2016; Ofir et al. 2018), so we model only the RVs for that system.

2.1. HIRES Observations

The radial velocity data for this work were collected using the HIRES spectrometer at the Keck Observatory from April 2010 to September 2017. The setup used for the RV observations was the same as used by the CPS (Howard et al. 2010), with a resolving power of $R \approx 60,000$ between wavelengths 3600 and 8000 Å (Marcy et al. 2008, 2014).

The Doppler analysis is the same as that used by the CPS group (Johnson et al. 2010). Template spectra obtained without the iodine cell were used to forward model the spectra taken with the iodine cell. The wavelength scale, the instrumental profile, and the RV in each of ~ 700 segments of length 80 pixels in length corresponding to ~ 2.0 Å (depending on position along each spectral order) are all solved for simultaneously. The internal uncertainty in the final RV measurement for each exposure is the weighted uncertainty in the mean RV of those segments, with weights inversely proportional to the relative RV scatter of each segment (Marcy et al. 2014).

To measure and remove contaminating light from the sky, we used the C2 decker on HIRES which has an $0''.87 \times 14''.0$ field of view on the sky. The C2 decker simultaneously collects both the stellar light and night-sky light, and the sky-contamination is recorded along with the stellar spectrum at each wavelength in the regions above and below each spectral order. These “sky pixels” provide a direct measurement of the sky spectrum at that wavelength and are subtracted from the stellar spectrum to mitigate sky contamination.

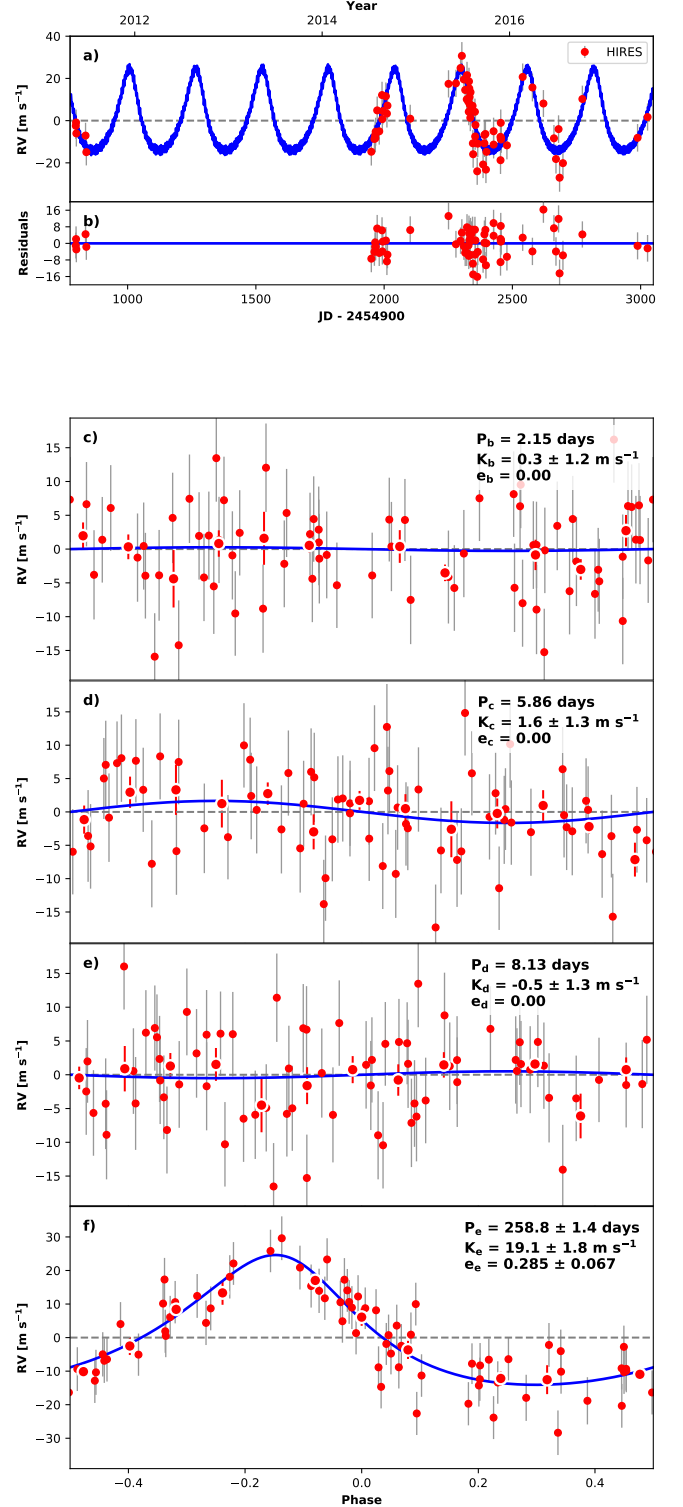


Figure 2. *Top Panel:* Kepler-65 RV *radvel* best-fit model and residuals. *Lower Panels:* RV data for each planet phase-folded at the best-fit orbital period with all other planet's signal removed.

Table 1. Kepler-65 MCMC Posteriors

Parameter ^a	Median ^{84th} Percentile ^{16th}	Unit
Fitted Parameters		
P_b	$2.1549209^{+8.6e-06}_{-7.4e-06}$	days
$T_{0,b}$	$801.32382^{+0.00011}_{-0.00011}$	BJD-2454900
$\sqrt{e} \cos \omega_b$	$-0.03^{+0.16}_{-0.15}$	
$\sqrt{e} \sin \omega_b$	$-0.02^{+0.12}_{-0.12}$	
i_b	$92.2^{+1.3}_{-1.4}$	degrees
M_b	$0.0076^{+0.0077}_{-0.0051}$	M_{Jupiter}
R_b/R_*	$0.009215^{+6.2e-05}_{-4.8e-05}$	
P_c	$5.859697^{+9.3e-05}_{-9.9e-05}$	days
$T_{0,c}$	$803.39284^{+0.00019}_{-0.00019}$	BJD-2454900
$\sqrt{e} \cos \omega_c$	$0.065^{+0.073}_{-0.112}$	
$\sqrt{e} \sin \omega_c$	$0.082^{+0.079}_{-0.09}$	
i_c	$92.33^{+0.29}_{-0.26}$	degrees
M_c	$0.017^{+0.0054}_{-0.0052}$	M_{Jupiter}
R_c/R_*	$0.016743^{+7.8e-05}_{-7.1e-05}$	
P_d	$8.13167^{+0.00024}_{-0.00021}$	days
$T_{0,d}$	$802.80285^{+0.00042}_{-0.00037}$	BJD-2454900
$\sqrt{e} \cos \omega_d$	$-0.05^{+0.11}_{-0.07}$	
$\sqrt{e} \sin \omega_d$	$0.01^{+0.1}_{-0.08}$	
i_d	$92.35^{+0.18}_{-0.16}$	degrees
Ω_d	$-0.13^{+0.76}_{-0.71}$	degrees
M_d	$0.013^{+0.0025}_{-0.0025}$	M_{Jupiter}
P_e	$258.8^{+1.5}_{-1.3}$	days
$T_{0,e}$	$1045.4^{+6.8}_{-8.2}$	BJD-2454900
$\sqrt{e} \cos \omega_e$	$0.492^{+0.067}_{-0.085}$	
$\sqrt{e} \sin \omega_e$	$0.16^{+0.12}_{-0.13}$	
i_e	$127.0^{+27.0}_{-25.0}$	degrees
Ω_e	$-10.0^{+130.0}_{-110.0}$	
M_e	$0.82^{+0.63}_{-0.16}$	M_{Jupiter}
M_*	$1.248^{+0.018}_{-0.021}$	M_{\odot}
R_*	$1.437^{+0.032}_{-0.027}$	R_{\odot}
c_1	$0.349^{+0.045}_{-0.047}$	
c_2	$0.227^{+0.067}_{-0.064}$	
σ_{jitter}	$6.05^{+0.75}_{-0.67}$	m s^{-1}
γ	$0.92^{+0.93}_{-0.92}$	m s^{-1}
Derived Parameters		
$M_{\text{jup},e} \sin i_e$	$0.653^{+0.056}_{-0.055}$	M_{Jupiter}
M_b	$2.4^{+2.4}_{-1.6}$	M_{\oplus}
M_c	$5.4^{+1.7}_{-1.7}$	M_{\oplus}
M_d	$4.14^{+0.79}_{-0.8}$	M_{\oplus}
M_e	$260.0^{+200.0}_{-50.0}$	M_{\oplus}
R_b	$1.444^{+0.037}_{-0.031}$	R_{\oplus}
R_c	$2.623^{+0.066}_{-0.056}$	R_{\oplus}
R_d	$1.587^{+0.040}_{-0.035}$	R_{\oplus}
ρ_b	$4.4^{+4.5}_{-3.0}$	g cm^{-3}
ρ_c	$1.64^{+0.53}_{-0.51}$	g cm^{-3}
ρ_d	$5.7^{+1.2}_{-1.2}$	g cm^{-3}
e_b	$0.028^{+0.031}_{-0.02}$	
e_c	$0.02^{+0.022}_{-0.013}$	
e_d	$0.014^{+0.016}_{-0.010}$	
e_e	$0.283^{+0.064}_{-0.071}$	

^aOsculating orbital elements are valid at $T_{\text{epoch}} = 2, 455, 715$ BJD.

2.2. Photometric Modeling

The *Kepler* photometry is prepared for dynamical fits by detrending the simple aperture photometry (SAP) flux data from the *Kepler* portal on the Mikulski Archive for Space Telescopes (MAST). For long-cadence data, we fit the amplitudes of the first five cotrending basis vectors away from transits to determine a baseline. We discard points whose quality flag had a value greater than or equal to 16. For short-cadence data, cotrending basis vectors are not available. For both cadences, we masked out the expected transit times plus 20% of the full duration of each transit to account for possible timing variations. We then fit a cubic polynomial model with a 1-day width centered within half an hour of each data point to determine its baseline. We divide the flux and uncertainties by this baseline. A small amount of correlated noise was still present in the data likely due to known spurious instrumental frequencies (García et al. 2011; Christiansen et al. 2013) and stellar variability. To avoid distorting the transit shapes, we do not attempt to detrend this short time-scale noise. We multiplied the normalized uncertainties from the *Kepler* data set by the $\sqrt{\chi^2_{\text{nom}}/N}$, where N is the number of data points in the *Kepler* data, and χ^2_{nom} is the χ^2 of a nominal best-fit model. Thus the reduced χ^2 of our best-fitting models was 1.00. By increasing our uncertainties, we conservatively widen our posteriors to take into account the scatter introduced by the aforementioned unmodeled noise in the system.

2.3. Fits Only Using Radial Velocities

For the radial velocity fits, we use **radvel** (Fulton et al. 2018), a Keplerian multi-planet radial velocity fitting routine. It is coupled to **emcee** (Foreman-Mackey et al. 2013), a Markov Chain Monte Carlo (MCMC) engine, so that Bayesian posteriors may be found. Each RV fit includes a radial velocity jitter term, σ_{jitter} to take into account stellar and instrumental noise above the measured uncertainty level (for details, see Fulton et al. 2018). The planets's orbits were fitted in a basis of $\{K, P, T_0, \sqrt{e} \cos \omega, \sqrt{e} \sin \omega\}$, where K is the radial velocity amplitude, P is the planetary period, T_0 is the time of planet-star conjunction, and e and ω are planetary eccentricity and argument of pericenter respectively. We use uniform priors on each parameter unless explicitly stated. For each model we run an MCMC to fit the data and determine uncertainties, stopping once all parameters have a Gelman-Rubin statistics of < 1.01 (Gelman & Rubin 1992). We convert the measured RV amplitudes into absolute planet masses by applying stellar mass constraints from Fulton & Petigura (2018).

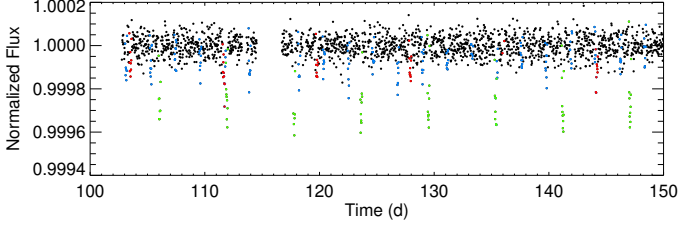


Figure 3. A segment of the long-cadence portion of Kepler-65’s detrended lightcurve (BJD-2454900) with transit events highlighted in blue (planet b), green (planet c), and red (planet d).

2.4. RV-TTV Fits

We use a photodynamic model to produce theoretical lightcurves for comparison to the *Kepler* photometry. The model takes initial conditions at a specified epoch, and integrates the N-body equations of motions of the planets over the interval of the data. If the integration reaches time of an RV data point, the stellar RV is computed by summing the effects of all planets at that instant. Every time a planet passes in front of the star, a theoretical lightcurve is computed at each *Kepler* time-series data point using the model described in Pál (2012). For long-cadence data, we computed the flux value at 15 equally spaced points in time over a cadence’s integration and averaged them together to produce the model value. The model and data are then compared in a χ^2 sense to compute the likelihood of the model, accounting for any priors for the parameters (specified for each system below). We perform a differential evolution (DE) MCMC (Ter Braak 2005) in order to understand the uncertainties of the system parameters.

The parameters for each planet in our model are the osculating Jacobian orbital elements P , T_0 , $\sqrt{e} \cos \omega$, $\sqrt{e} \sin \omega$, i , Ω , M/M_\star , and R/R_\star , where Ω is the longitude of the ascending node, and M and R are mass and radius respectively. We model the star with four free parameters: R_\star , M_\star , and two quadratic limb-darkening parameters c_1 and c_2 , following Pál (2012). σ_{jitter} is a final free parameter.

3. KEPLER-65

Kepler-65 (KOI 85, KIC 5866724) is a system of three transiting planets all with $R < 3R_\oplus$ and orbital periods < 10 days as originally validated by Chaplin et al. (2013). Chaplin et al. (2013) showed that the inner planets’ orbits are aligned with the spin of the star. Hadden & Lithwick (2014) marginally detected a TTV signal which implies a non-zero mass for planet c using the first 12 quarters of long-cadence data (Mazeh et al. 2013). HIRES RV data revealed an additional companion which

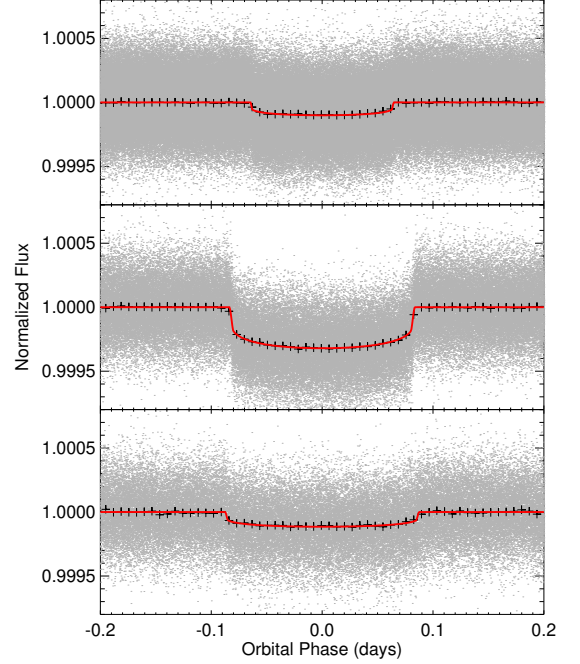


Figure 4. Kepler-65’s three transiting planets b, c, and d are show from top to bottom phase-folded with TTVs removed. Gray points are individual *Kepler* data, black crosses are data binned in 10 minute intervals, and the red line is a best fit transit model.

we denote with the subscript e at an orbital period of $258.7^{+1.5}_{-1.3}$ days and $M \sin i$ of $0.67 \pm 0.06 M_{\text{Jupiter}}$. Below we explore a fit to the radial velocities alone and to the photometry and RVs simultaneously for higher precision determination of the system’s architecture.

3.1. Kepler-65 RV Only Fit

We perform a Keplerian RV fit with *radvel* (Fulton et al. 2018) on the HIRES RV data set (Table 8). The inner planets have well determined orbital periods from *Kepler*. Additionally, they are likely to have low eccentricities (Van Eylen & Albrecht 2015), so in this preliminary RV-only fit we fix their eccentricities to 0 to prevent degeneracies with mass. Therefore the only free parameters for the inner 3 planets are the K amplitudes (i.e., their masses). We allow all parameters of the newly discovered outer planet to vary (P , T_0 , $\sqrt{e} \sin \omega$, $\sqrt{e} \cos \omega$, K). Our best fit model is shown in Fig. 2. None of the inner planets are detected at high significance. However, the non-transiting planet is detected at $> 10\sigma$ significance, and the departure from a perfectly sinusoidal shape of the outer planet’s RV signal reveals a significant eccentricity ($e = 0.286 \pm 0.069$). We note that removing

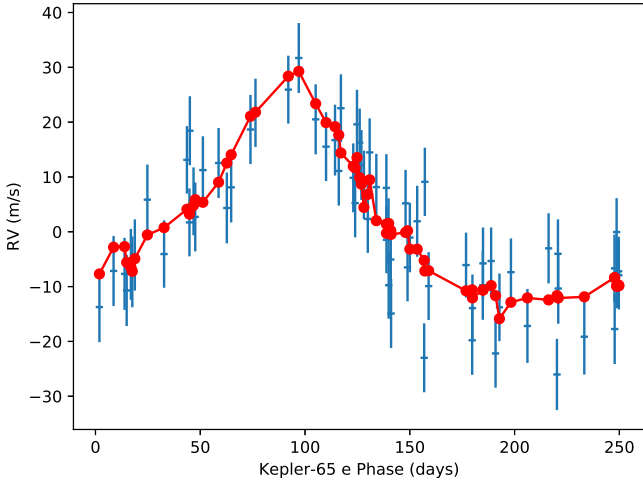


Figure 5. Kepler-65’s best RV fit (red) and the HIREs RV data (crosses with uncertainties including the best-fit RV jitter of 5.3 m s^{-1}) phased at the best-fit orbital period of the long-period giant planet e. The small amplitude variations in the theoretical points is due to the RV contribution of the 3 inner planets, whose RV signatures are no longer completely periodic in an N-body model. Their low amplitudes agree with the RV-only fit. The deviation of the large-amplitude shape from a sine curve belies the eccentricity in the giant planet.

the giant planet’s eccentricity in the RV fit results in an increase in the Akaike Information Criteria by 12.1, which is sufficient to strongly rule out the $e = 0$ model (Akaike 1974; Burnham & Anderson 2002).

We note that a Lomb-Scargle (LS) periodogram (Lomb 1976; Scargle 1982) of the data indicates a unique, well defined peak at 259 days, eliminating the possibility the observed periodicity is an alias for a different period of the giant planet induced by the time sampling. We also consider stellar activity as a potential false positive for an apparent planetary signal. A periodogram of the S-values of the HIREs RV data does not show a peak at the period of the putative planet and there is almost no correlation ($\rho = 0.03$) between the S-value stellar activity indicator and the RV signal. $\log(R'_{\text{HK}}) = -5.178 \pm 0.052$, consistent with low stellar activity. We also note that a LS periodogram of the RV data suggests there is no significant periodicity remaining after subtracting a best-fit with the three known planets. We inject additional planets on circular orbits, and recover them with an LS periodogram. We find that planets with a K amplitude $> 7 \text{ m s}^{-1}$ are ruled out at the $2\text{-}\sigma$ level with periods from 55 to 1800 days. This corresponds to a $0.5 M_{\text{Jupiter}}$ planet in a 5 year

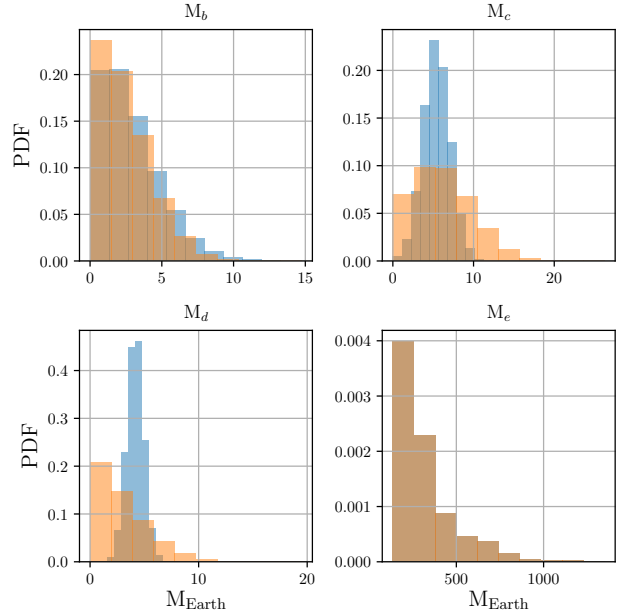


Figure 6. Mass posteriors for all planets in the Kepler-65 system from the joint RV-*Kepler* photometry fit (blue) and from RVs alone (orange). While the inner planet (b) has an upper limit from RVs alone, the addition of the transit timing variations significantly improves the precision of planet c and d’s masses.

orbit, with more stringent mass constraints for shorter periods. Any proposed mechanism for the excitation of eccentricity of planet e to its observed value, must account for this constraint.

3.2. Photometry and RV Simultaneous Fit

We next perform a photodynamic fit including both the HIREs RV data and all quarters of *Kepler* photometry data detrended as described in §2. We include all 18 quarters of *Kepler* data including the 15 containing short cadence (58 second integration) data, which is vital for resolving transit ingress and egress and thus precise transit times. A segment of the long cadence lightcurve with transits highlighted is shown in Fig. 3. Planets c and d are near a 7:5 resonance with potential TTVs of ~ 5 minutes assuming modest eccentricities ($e \lesssim 0.05$) as calculated using the formalism in Deck & Agol (2016).

Our model follows that described in §2.4. Additionally, we fix $\Omega = 0$ for the inner three planets since their mutual inclinations are not well-constrained by the data but the planets are likely nearly coplanar due the fact that all three transit. We allow Ω_e to vary to test if the data constrain the mutual inclination between the compact inner planets and the outer giant planet. This

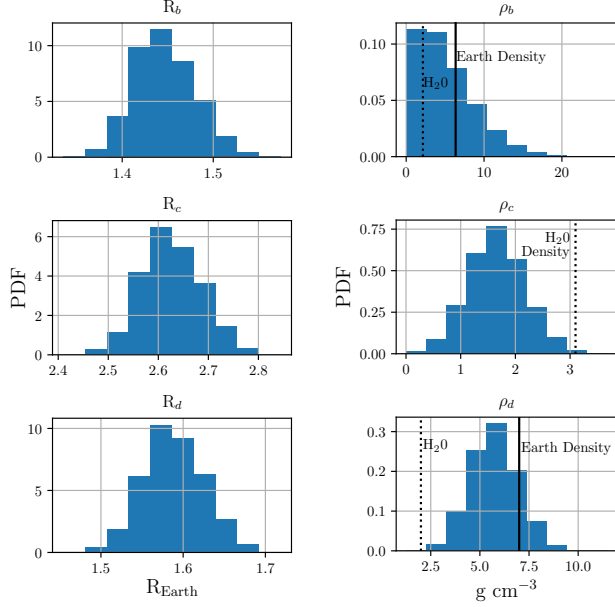


Figure 7. Radius and density posteriors of the transiting planets in the Kepler-65 system from the joint RV-*Kepler* photometry fit. The theoretical density of an Earth-composition planet of the observed radius is shown as a solid vertical line (Dressing et al. 2015). A dotted vertical line indicates the density of a 100% water planet, essentially indicating lower bound on the density of a planet without an H/He atmosphere contributing significantly to the observed radius. Since planet c lies entirely below the H₂O density, it must have a significant H/He envelope, while planet d’s allowed densities are consistent with a wider range of compositions.

choice also allows the posteriors of all other fitted parameters to marginalize over the uncertainty in Ω_e . We fix $R_e = 0.01R_*$ since it is unconstrained by the data, except that the planet does not produce significant transits. We apply a half Gaussian e prior on the inner 3 planets with $\sigma_e = 0.05$. This is justified since compact multiply transiting systems of small planets have low eccentricities (Van Eylen & Albrecht 2015; Xie et al. 2016). On the other hand, the giant planet is given a uniform e prior due to the wide range of eccentricities in massive long-period planets. We apply a $\sin i$ geometric prior on the planetary inclinations. Results of a 60 chain differential evolution Markov chain Monte Carlo (DE-MCMC) simulation (Ter Braak 2005) run for 300,000 generations after burn-in are shown in Figs. 4, 5, 6, and 7 and summarized in Table 1. This DEMCMC was stopped when the Gelman-Rubin statistic was < 1.2 for all parameters and the chains remained stationary, indicating no upward or downward trends with time and no spreading (i.e., the parameter distributions for the first 150,000 generations are similar to the final 150,000 gen-

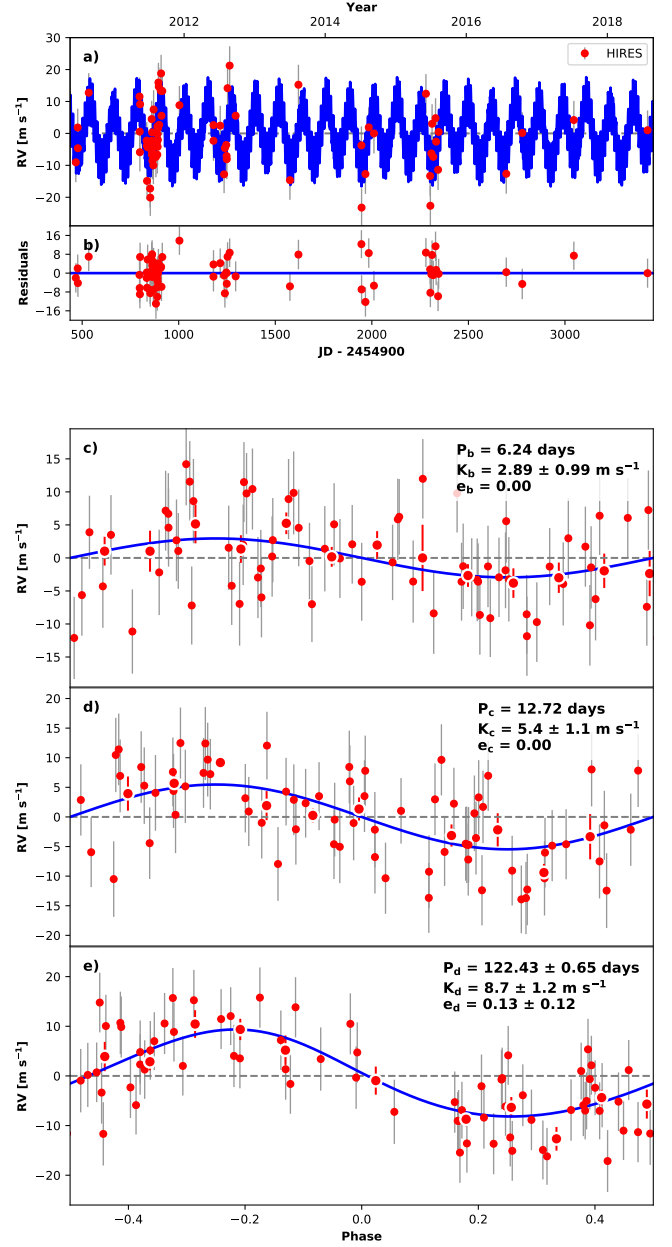


Figure 8. Top Panel: Kepler-25 RV *radvel* best-fit model and residuals. Lower Panels: RV data for each planet phase-folded at the best-fit orbital period with all other planet’s signal removed.

erations). Fig. 14 illustrates the degeneracies between the derived masses and eccentricities of the planets via a corner plot of the appropriately transformed DEMCMC parameters.

3.3. Kepler-65 Discussion

Table 2. Kepler-25 Model Comparison

AICc Qualitative Comparison	Free Parameters	N_{free}^a	N_{data}	RMS	$\ln \mathcal{L}$	BIC	AICc	ΔAICc
AICc Favored Model	$K_b, K_c, K_d, \sigma_{\text{jitter}}, \gamma$	7	71	6.14	-235.90	501.64	487.58	0.00
Strongly Disfavored	$K_b, K_c, e_d, K_d, \sigma_{\text{jitter}}, \gamma$	9	71	6.10	-235.51	509.38	491.97	4.39
	$K_c, K_d, \sigma_{\text{jitter}}, \gamma$	6	71	6.55	-240.51	506.60	494.34	6.76
Ruled Out	$K_b, K_d, \sigma_{\text{jitter}}, \gamma$	6	71	7.28	-248.42	522.41	510.14	22.56
	$K_b, K_c, \sigma_{\text{jitter}}, \gamma$	4	71	8.65	-260.70	538.44	530.00	42.42

^a P_d and $T_{0,d}$ are allowed to vary whenever K_d is a free parameter. Each e also encodes two free parameters: $\sqrt{e} \cos \omega$ and $\sqrt{e} \sin \omega$.

The radii of planets b, c, and d span the observed short period exoplanet radius gap, a minimum in the planetary radius distribution between that occurs at $\approx 1.8R_{\oplus}$ (Fulton et al. 2017). This gap is thought to divide high-density super-Earths and low-density sub-Neptunes due to photo-evaporation (Owen & Wu 2013, 2017). Planet c’s relatively large radius ($R = 2.623_{-0.056}^{+0.066} R_{\oplus}$) combined with its low density ($\rho_c = 1.64_{-0.51}^{+0.53} \text{ g cm}^{-3}$; see Fig. 7) suggests it may have been able to maintain a significant fraction of its primordial gas envelope. The density and uncertainties ($\rho_d = 5.7 \pm 1.2 \text{ g cm}^{-3}$) of planet d are consistent with it either having a rocky composition or possessing H/He envelope despite its small radius ($R_d = 1.587 \pm 0.04 R_{\oplus}$). The former is preferred by photo-evaporation models which suggest the planet should be rocky since it receives ~ 400 times the Earth’s incident flux (Lopez & Rice 2018). For comparison, an Earth-composition planet of planet d’s radius is expected to have a density of 7 g cm^{-3} (Dressing et al. 2015). Owen & Wu (2013) demonstrate that for solar-like stars, core masses of $\sim 6\text{--}8M_{\oplus}$ at planet’s c and d’s semi-major axes (0.69 AU and 0.85 AU respectively) undergo a transition from low-density planets with envelopes to bare cores. Although planet c receives more stellar flux than planet d, it is up to 80% more massive at the 1- σ level. If planet c’s mass is indeed on the higher end of the derived posteriors, it is thus consistent with the photo-evaporation picture due to the strong $M^{2.4}$ dependence on the necessary flux to erode an atmosphere (Lopez & Fortney 2013). Planet b’s density and composition remains mostly unconstrained. Parameters of the outer giant planet e are somewhat uncertain due to the RV data alone constraining its orbital parameters, however its mass is $\gtrsim 0.6M_{\text{Jupiter}}$ and its eccentricity is 0.28 ± 0.07 , higher than most planets in multi-planet systems (see Fig. 5). We note that no other giant planets ($M > 0.5M_{\text{Jupiter}}$) within a factor of 5 in orbital period of planet e are present in the system, determined from the lack of additional periodic RV signals. The

mutual inclination between the outer giant planet e and the inner 3 planets is not meaningfully constrained by the data.

4. KEPLER-25

Kepler-25 (KOI-244, KIC 4349452) is a system of two transiting planets between 2 and 5 R_{\oplus} and with orbital periods near a 2:1 ratio at 6.2 and 12.7 days (Steffen et al. 2012). Marcy et al. (2014) use RVs to identify an additional non-transiting $\sim 90M_{\oplus}$ companion on a 123 day orbit. We use additional HIRES RV observations and an extended time baseline to more precisely characterize both the inner transiting planets and the outer non-transiting planet. The inner planets both exhibit TTVs (Steffen et al. 2012; Holczer et al. 2016). The TTVs were used to estimate the planetary masses by Hadden & Lithwick (2017) who found $M_b = 4_{-2}^{+4} M_{\oplus}$ and $M_c = 10_{-2.5}^{+3.5} M_{\oplus}$ subject to a high mass prior and $M_b = 0.4_{-0.2}^{+1.5} M_{\oplus}$ and $M_c = 1.4_{-0.6}^{+4} M_{\oplus}$ with a less informative prior. By combining the RV data and the photometric data simultaneously, we put more precise mass and density constraints on the inner planets.

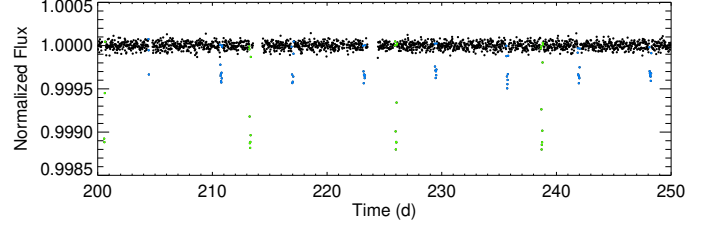
Albrecht et al. (2013) demonstrate that planet c’s orbit is nearly aligned with the host star rotation (i.e., it has obliquity $\lesssim 22^\circ$) via a 2-night Rossiter-McLaughlin (R-M) measurement. For our RV fit, we include HIRES RVs made as part of the CPS survey (Howard et al. 2010) and choose to include only two RV measurements of the system on the nights of the R-M observations (before and after each transit). Hence the R-M effect does not bias our fit, and any correlated noise on the ~ 12 hour timescale of the observations does not get unfairly favored by the density of observations on these nights. The complete list of the RV data used for this fit is given in Table 7.

The dynamics of the inner transiting planets of Kepler-25 were also studied in detail by Migaszewski & Goździewski (2018). They stated that the system is consistent with either being in a periodic (resonant) con-

Table 3. Kepler-25 MCMC Posteriors

Parameter ^a	Median _{84th Percentile} 16 th Percentile	Unit
Fitted Parameters		
P_b	$6.238297^{+1.7e-05}_{-1.7e-05}$	days
$T_{0,b}$	$803.42004^{+0.00012}_{-0.00011}$	BJD-2454900
$\sqrt{e} \cos \omega_b$	$0.042^{+0.017}_{-0.036}$	
$\sqrt{e} \sin \omega_b$	$0.007^{+0.038}_{-0.035}$	
i_b	$92.827^{+0.084}_{-0.083}$	degrees
M_b	$0.0275^{+0.0079}_{-0.0073}$	M_{Jupiter}
$R_p/R_{\star b}$	$0.01916^{+5.1e-05}_{-4.8e-05}$	
P_c	$12.7207^{+0.00011}_{-0.0001}$	days
$T_{0,c}$	$811.15013^{+0.00014}_{-0.00014}$	BJD-2454900
$\sqrt{e} \cos \omega_c$	$-0.024^{+0.067}_{-0.053}$	
$\sqrt{e} \sin \omega_c$	$0.004^{+0.065}_{-0.062}$	
i_c	$92.764^{+0.042}_{-0.039}$	degrees
Ω_c	$-0.45^{+0.19}_{-0.25}$	degrees
M_c	$0.0479^{+0.0041}_{-0.0051}$	M_{Jupiter}
$R_p/R_{\star c}$	$0.03637^{+0.00012}_{-0.00012}$	
P_d	$122.4^{+0.8}_{-0.71}$	days
$T_{0,d}$	$815.0^{+6.8}_{-7.2}$	BJD-2454900
$\sqrt{e} \cos \omega_d$	$0.07^{+0.27}_{-0.29}$	
$\sqrt{e} \sin \omega_d$	$0.16^{+0.23}_{-0.28}$	
M_d	$0.226^{+0.031}_{-0.031}$	M_{Jupiter}
M_{\star}	$1.165^{+0.027}_{-0.029}$	M_{\odot}
R_{\star}	$1.316^{+0.016}_{-0.015}$	R_{\odot}
c_1	$0.351^{+0.049}_{-0.051}$	
c_2	$0.198^{+0.056}_{-0.055}$	
σ_{jitter}	$5.44^{+0.74}_{-0.65}$	m s^{-1}
γ	$1.67^{+0.85}_{-0.88}$	m s^{-1}
Derived Parameters		
i_c/i_b	$0.99932^{+0.0005}_{-0.00048}$	
M_b	$8.7^{+2.5}_{-2.3}$	M_{\oplus}
M_c	$15.2^{+1.3}_{-1.6}$	M_{\oplus}
M_d	$71.9^{+9.8}_{-9.8}$	M_{\oplus}
$M_d \sin i_d$	$0.226^{+0.031}_{-0.031}$	M_{Jupiter}
R_b	$2.748^{+0.038}_{-0.035}$	R_{\oplus}
R_c	$5.217^{+0.07}_{-0.065}$	R_{\oplus}
ρ_b	$2.32^{+0.67}_{-0.61}$	g cm^{-3}
ρ_c	$0.588^{+0.053}_{-0.061}$	g cm^{-3}
e_b	$0.0029^{+0.0023}_{-0.0017}$	
e_c	$0.0061^{+0.0049}_{-0.0041}$	
e_d	$0.13^{+0.13}_{-0.09}$	

^aOsculating orbital elements are valid at $T_{\text{epoch}} = 2,455,700$ BJD.

**Figure 9.** A segment of the long-cadence portion of Kepler-25's detrended lightcurve (BJD-2454900) with transit events highlighted in blue (planet b) and green (planet c).

figuration or not within the uncertainties in the planets' eccentricities. Although somewhat far from resonance with a period ratio of 2.039, the divergence of the resonance width at low eccentricity permits a periodic solution for $e \lesssim 0.002$ and relatively high planetary mass to reproduce the observed TTV amplitudes. The addition of our RV data set reduces the mass-eccentricity degeneracy found in the TTVs alone.

4.1. Kepler-25 RV Only Fit

We first perform a Keplerian fit with `radvel` on the HIRES RV data set alone (Table 7). The two inner planets have well determined orbital periods and phases from *Kepler*, which we fix at the observed values. As with Kepler-65, we set $e = 0$ and allow all parameters of the newly discovered outer planet to vary. Our best fit model is shown in Fig. 8. All three planets are detected at high significance (Table 2). We also note that eccentricity is not confidently detected in planet d since including e_d is disfavored by the AICc (small-sample corrected Akaike Information Criteria; Burnham & Anderson 2002), and is constrained to $e_d < 0.28$ at the 1- σ level if included³.

In addition to the most significant peak at 123 days in an LS Periodogram of the RVs, we note a secondary peak at 91 days with less power. A model comparison of a Keplerian RV fit with the outer planet at a 90 day orbital period compared to a 123 day period fit has a Δ Bayesian Information Criterion (BIC) = 6 (that is, a log likelihood difference of 4 for 7 free parameters), providing substantial evidence against the 91 day period, but not conclusively ruling it out. We emphasize that the RV posteriors for planets b and c are statistically similar between fits with the outer giant at a 90 days and a 123 days—the mass posteriors for both b and c are consistent to $< 0.5\sigma$ between the fits. Therefore the

³ This model comparison feature is freely available as part of the `radvel` package (<https://github.com/California-Planet-Search/radvel>).

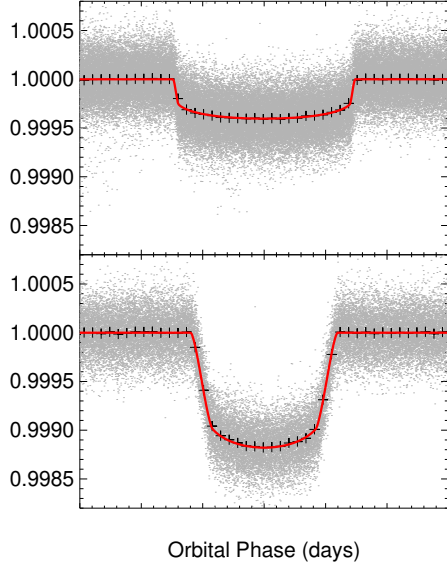


Figure 10. Kepler-25’s planets b (top) and c (bottom) phase-folded with TTVs removed. Gray points are individual *Kepler* data, black crosses are data binned in 10 minute intervals, and the red line is a best fit transit model.

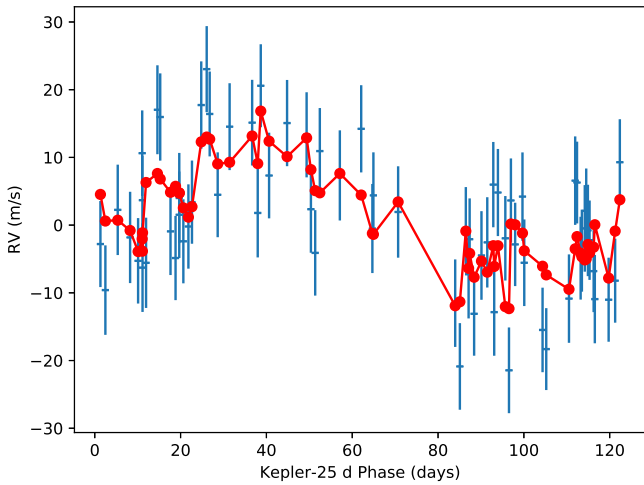


Figure 11. The best-fit solution’s theoretical RVs (red) and the HIRES RV data (crosses with uncertainties including the best-fit RV jitter of 5.3 m s^{-1}) phased at the best-fit orbital period of the long-period giant planet (planet d) in Kepler-25. The small amplitude variation in theoretical points is due to the RV contribution of the two inner planets. Their low amplitudes and correlation with variations in the data agree with the fit using only RVs.

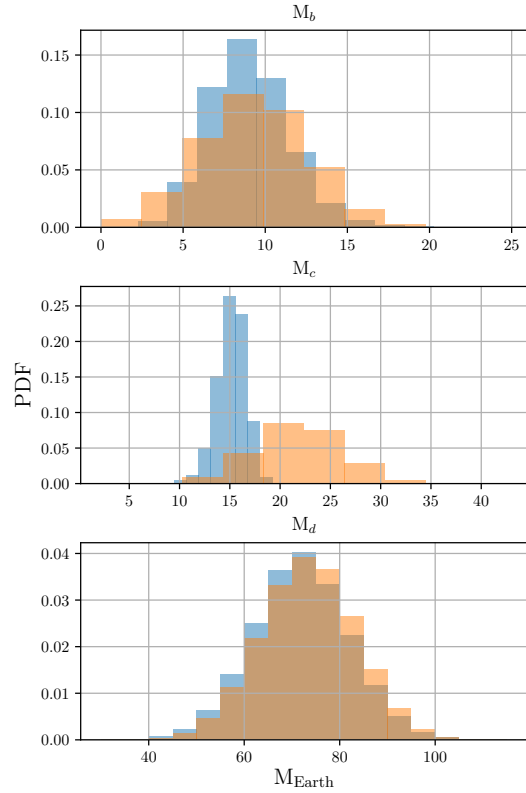


Figure 12. Mass posteriors for all planets in Kepler-25 from the joint RV-*Kepler* photometry fits (blue) and the RVs alone (orange). The precision of planet c’s mass increases dramatically with the addition of the TTV information, and the RVs indicate that the mass is at the higher end of the distribution allowed by the TTVs alone (Migaszewski & Goździewski 2018).

interpretation of the inner planets properties would not qualitatively change, even if the outer giant planet is indeed at the disfavored 91 day orbital period.

We also consider stellar activity as a potential false positive for an apparent planetary signal. A periodogram of the S-values of the HIRES RV data does not show a peak at the period of the putative outer planet. $\log(R'_{\text{HK}}) = -5.21 \pm 0.15$, consistent with low stellar activity. We also note that a LS periodogram suggests there is no significant periodicity remaining after subtracting a best-fit with the three known planets. We attempt to inject an additional planet on a circular orbits, and recover it with an LS periodogram. We find that planets with a K amplitude $> 7 \text{ m s}^{-1}$ are ruled out at the $2\text{-}\sigma$ level with periods from approximately 60 to 3000 days.

Table 4. Kepler-68 *radvel* MCMC Posteriors

Parameter	Credible Interval	Units
Orbital Parameters		
P_b	$\equiv 5.3988$	days
$T_{0,b}$	$\equiv 803.2978$	BJD-2454900
e_b	$\equiv 0.0$	
ω_b	$\equiv 0.0$	radians
K_b	$2.7^{+0.48}_{-0.46}$	m s^{-1}
P_c	$\equiv 9.6051$	days
$T_{0,c}$	$\equiv 808.9682$	BJD-2454900
e_c	$\equiv 0.0$	
ω_c	$\equiv 0.0$	radians
K_c	$0.59^{+0.50}_{-0.52}$	m s^{-1}
P_d	$634.6^{+4.1}_{-3.7}$	days
$T_{0,d}$	978 ± 11	BJD-2454900
e_d	$0.112^{+0.035}_{-0.034}$	
ω_d	$-1.13^{+0.36}_{-0.45}$	radians
K_d	$17.75^{+0.50}_{-0.49}$	m s^{-1}
Other Parameters^a		
γ_{HIRES}	$1.85^{+0.74}_{-0.72}$	m s^{-1}
$\dot{\gamma}$	$-0.00319^{+0.00075}_{-0.00078}$	$\text{m s}^{-1} \text{ d}^{-1}$
$\ddot{\gamma}$	$-3.23e-06^{+8.6e-07}_{-8.3e-07}$	$\text{m s}^{-1} \text{ d}^{-2}$
σ_{jitter}	$2.93^{+0.32}_{-0.29}$	m s^{-1}
Derived Parameters^b		
$M_b \sin i$	$7.65^{+1.37}_{-1.32}$	M_{\oplus}
$M_c \sin i$	$2.04^{+1.72}_{-1.78}$	M_{\oplus}
$M_d \sin i$	$0.77^{+0.03}_{-0.03}$	M_{Jupiter}

^a Reference epoch for $\gamma, \dot{\gamma}, \ddot{\gamma}$: 2000

^b With system scale set using stellar data from (Fulton & Petigura 2018).

4.2. Photometry and RV Simultaneous Fit

The TTVs detected between the two transiting planets (Hadden & Lithwick 2017; Holczer et al. 2016) present a degeneracy between their masses and eccentricities (Lithwick et al. 2012; Migaszewski & Goździewski 2018). Including the RV data may help break this degeneracy as the RVs can put bounds on the allowed masses. Therefore we perform a photodynamic fit including both the HIRES RV data simultaneously and all quarters of *Kepler* photometry data (a segment of which is shown in Fig. 9).

We fix $\Omega_b = 0$, but allow Ω_c to vary since we expect the inner two planets to be tightly coupled and therefore have mutual inclination well-constrained by the TTVs

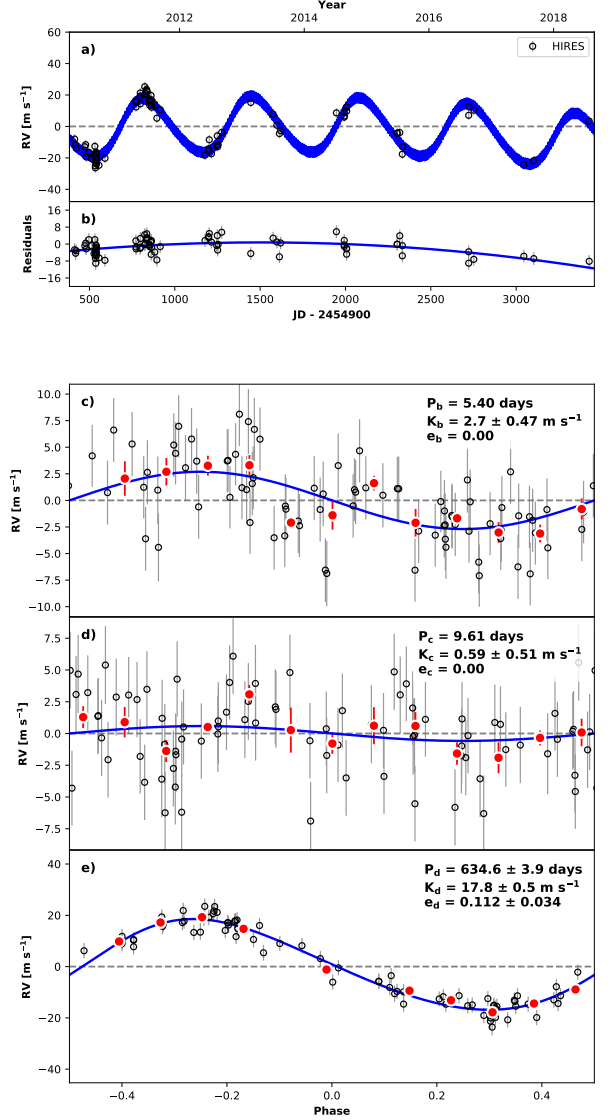


Figure 13. Top Panel: Kepler-68 RV *radvel* best-fit model and residuals. Lower Panels: RV data for each planet phase-folded at the best-fit orbital period with all other planet's signal removed.

and lack of large duration variations (TDVs). We also fix $R_d = 0.01 R_{\star}$ since it is completely unconstrained by the data and does not affect our fits except that the planet should not produce significant transits since none are observed.

Similar to the Kepler-65 fit, we apply a Gaussian e prior on the inner two planets with $\sigma_e = 0.05$, and also note that Kepler-25's planets must have eccentricities well within that range for any physical masses (Migaszewski & Goździewski 2018). On the other hand,

Table 5. Kepler-68 Model Comparisons

AICc Qualitative Comparison	Free Parameters ^a	N_{free}^b	N_{data}	RMS	$\ln \mathcal{L}$	BIC	AICc	ΔAICc
AICc Favored Model	$K_b, e_d, K_d, \dot{\gamma}, \ddot{\gamma}, \sigma_{\text{jitter}}, \gamma$	10	82	3.05	-224.92	493.91	472.94	0.00
Nearly Indistinguishable	$K_b, K_c, e_d, K_d, \dot{\gamma}, \ddot{\gamma}, \sigma_{\text{jitter}}, \gamma$	11	82	3.03	-224.19	496.86	474.16	1.22
Strongly Disfavored	$K_b, K_d, \dot{\gamma}, \ddot{\gamma}, \sigma_{\text{jitter}}, \gamma$	8	82	3.29	-231.15	497.55	480.27	7.33
	$K_b, K_c, K_d, \dot{\gamma}, \ddot{\gamma}, \sigma_{\text{jitter}}, \gamma$	9	82	3.27	-230.60	500.86	481.70	8.76
Ruled Out	$K_b, e_d, K_d, \dot{\gamma}, \sigma_{\text{jitter}}, \gamma$	9	82	3.33	-231.99	503.64	484.48	11.54
	$K_b, K_c, e_d, K_d, \dot{\gamma}, \sigma_{\text{jitter}}, \gamma$	10	82	3.32	-231.68	507.43	486.46	13.52
	$K_b, e_d, K_d, \sigma_{\text{jitter}}, \gamma$	8	82	3.44	-234.90	505.06	487.78	14.84
	$K_b, K_c, e_d, K_d, \sigma_{\text{jitter}}, \gamma$	9	82	3.44	-234.73	509.13	489.97	17.03

^a P_d and $T_{0,d}$ are allowed to vary whenever K_d is a free parameter. Each e also encodes two free parameters: $\sqrt{e} \cos \omega$ and $\sqrt{e} \sin \omega$.

the giant planet has a uniform e prior due to the wide range of eccentricities in massive long-period planets. We again apply stellar mass and radius data from [Fulton & Petigura \(2018\)](#) as priors to get absolute radius and density information for the system. The planetary masses and other parameters are all given a uniform prior.

We consider allowing Ω_d and i_d to vary, but find that our fits slightly favor a highly mutually inclined configuration ($I \gtrsim 30^\circ$) under a uniform Ω prior and a geometric $\sin i$ prior. However the improvement in the likelihood is small, compared to the introduction of free parameters. We compare the models using the BIC (Bayesian Information Criteria) and AICc. Specifically, the $\Delta\text{BIC} = -13$ favors the extra free parameters while the $\Delta\text{AIC} = 12$ disfavors them, suggesting that it is not clear if the addition of the inclination parameters is well-founded in our model given the data. Therefore in our final fit reported here, we fix $\Omega_d = \Omega_b = 0$ and $i_d = 92^\circ \approx i_b \approx i_c$, since the data may be insufficient to determine mutual inclination and most known multi-planet systems are nearly coplanar ([Fabrycky et al. 2014](#); [Zhu et al. 2018](#)). We expect this choice to have little effect on the posteriors of other parameters in our model and will prevent misleading high mutual inclination fits from dominating the reported posteriors.

Results of a 40 chain DEMCMC ([Ter Braak 2005](#)) run for 220,000 generations after burn-in are shown in Figs. 10, 11, and 12 and summarized in Table 3. This MCMC was stopped when the Gelman-Rubin statistic was < 1.2 for all parameters and the chains remained stationary, indicating no upward or downward trends with time and no spreading (i.e., the parameter distributions for the first 110,000 generations are similar to the final 110,000 generations). Fig. 15 illustrates the degeneracies between the derived masses and eccentrici-

ties of the planets via a corner plot of the appropriately transformed DEMCMC parameters.

4.3. Kepler-25 Discussion

Our RV-TTV combined results favor high masses and low eccentricities (see Fig. 12) compared to the range of possible values as explored in [Migaszewski & Goździewski \(2018\)](#). This is primarily due to the RV signal, whose relatively large amplitudes partially break the TTV mass-eccentricity degeneracy. Our results are within 1-2 σ of the [Hadden & Lithwick \(2017\)](#) result when a high mass prior was used. The low eccentricities found are consistent with the low-eccentricity resonant state that [Migaszewski & Goździewski \(2018\)](#) speculate Kepler-25 occupies; however, our results do not strictly demand resonance.

5. KEPLER-68

The two transiting planets detected by *Kepler* and one non-transiting planet detected via RVs in Kepler-68 (KOI-246, KIC 11295426) were validated by [Gilliland et al. \(2013\)](#). The non-transiting outer planet was found by [Marcy et al. \(2014\)](#), who report $P_d = 625 \pm 16$ days and $M_d \sin i = 0.84 \pm 0.05 M_{\text{Jupiter}}$. Here we provide improved constraints from additional RV data and a longer time baseline. Since the transiting planets exhibit no TTVs, we only fit the RV data (shown in full in Table 9). We again run a `radvel` fit with the inner planets' periods and phases fixed based on the *Kepler* data. The results of an MCMC are summarized in Table 4, with the best fit shown in Fig. 13. We note that the mass posteriors are symmetric, Gaussian, and have no apparent correlation with any other parameters.

We consider several different models of the RV data with and without terms for a linear trend, quadratic curvature, and eccentricity for the outer planet and com-

pare their relative likelihoods via BIC and AICc. Our results in Table 5 show that the inclusion of both the long-timescale curvature terms (linear and quadratic) and planet d’s eccentricity are both strongly preferred. The presence of curvature in the RVs indicates the presence of another body in the system at a period $\gtrsim 10$ years and uncertain mass. This could either be a planetary or stellar companion. At the ~ 10 year period lower limit, the signal would correspond to a planetary $M \sin i$ of $\sim 0.6 M_{\text{Jupiter}}$, however the period and mass of this body are not bounded by the measurements and could be much greater. Ginski et al. (2016) report a nearby star in a lucky imaging survey for companions at a distance of 11". They conclude the companion is likely bound to Kepler-68; however, this star is at such a great distance from Kepler-68 (≈ 1600 AU sky-projected; Gaia Collaboration et al. 2018) that it is not likely the cause of the observed curvature in the RVs. A circular orbit with the sky-projected distance as the semi-major axis would have $P \sim 50,000$ years, which would not be detectable over our ~ 7 -year baseline.

A periodogram of the S-values of the HIRES RV data does not show a peak at the period of the putative planet or its harmonics. The presence of some additional weak peaks in the S-value periodogram are taken into account by the model’s stellar jitter term which appropriately broadens the posteriors of the derived planetary properties. There is only weak correlation between the stellar activity indicator and the RV signal ($\rho = -0.2$). This correlation is driven in part by a single point with anomalously low S-value which provides a large lever when fitting a linear correlation which we suspect is due to sky background contamination, so we do not expect our results to be significantly biased by stellar activity. Additionally, $\log(R'_{\text{HK}}) = -5.153 \pm 0.037$, consistent with low stellar activity.

6. SUMMARY AND DISCUSSION

In this paper we expand the sample of known long-period giant planet companions to compact, coplanar, multiply-transiting systems with the introduction of the $M \sin i = 0.65 \pm 0.06 M_{\text{Jupiter}}$ Kepler-65 e. Additionally, we provide improved mass and orbital element constraints on the long-period Jupiters in Kepler-25 and Kepler-68, while also tentatively suggesting the presence of a second long-period companion in Kepler-68 with $P \gtrsim 10$ years. Important system parameters are summarized in Table 6. The non-transiting giant planets in all 3 systems are dynamically separated from the inner SEASNs due to their large orbital period ratios (approximately 9.6, 32, and 66 in Kepler-25, Kepler-65, and Kepler-68 respectively). Our joint RV-TTV analysis

Table 6. System Summaries

Parameter	Credible Interval	Units
Kepler-25		
P_b	$6.238297^{+1.7e-05}_{-1.7e-05}$	days
P_c	$12.7207^{+0.00011}_{-0.0001}$	days
P_d	$122.4^{+0.80}_{-0.71}$	days
M_b	$8.7^{+2.5}_{-2.3}$	M_{\oplus}
M_c	$15.2^{+1.3}_{-1.6}$	M_{\oplus}
$M_d \sin i_d$	$0.226^{+0.031}_{-0.031}$	M_{Jupiter}
R_b	$2.748^{+0.038}_{-0.035}$	R_{\oplus}
R_c	$5.217^{+0.07}_{-0.065}$	R_{\oplus}
ρ_b	$2.32^{+0.67}_{-0.61}$	g cm^{-3}
ρ_c	$0.588^{+0.053}_{-0.061}$	g cm^{-3}
e_b	$0.0029^{+0.0023}_{-0.0017}$	
e_c	$0.0061^{+0.0049}_{-0.0041}$	
e_d	$0.13^{+0.13}_{-0.09}$	
Kepler-65		
P_b	$2.1549209^{+8.6e-06}_{-7.4e-06}$	days
P_c	$5.859697^{+9.3e-05}_{-9.9e-05}$	days
P_d	$8.13167^{+0.00024}_{-0.00021}$	days
P_e	$258.8^{+1.5}_{-1.3}$	days
M_b	$2.4^{+2.4}_{-1.6}$	M_{\oplus}
M_c	$5.4^{+1.7}_{-1.7}$	M_{\oplus}
M_d	$4.14^{+0.79}_{-0.8}$	M_{\oplus}
$M_e \sin i_e$	$0.653^{+0.056}_{-0.055}$	M_{Jupiter}
R_b	$1.444^{+0.037}_{-0.031}$	R_{\oplus}
R_c	$2.623^{+0.066}_{-0.056}$	R_{\oplus}
R_d	$1.587^{+0.04}_{-0.035}$	R_{\oplus}
ρ_b	$4.4^{+4.5}_{-3.0}$	g cm^{-3}
ρ_c	$1.64^{+0.53}_{-0.51}$	g cm^{-3}
ρ_d	$5.7^{+1.2}_{-1.2}$	g cm^{-3}
e_b	$0.028^{+0.031}_{-0.02}$	
e_c	$0.02^{+0.022}_{-0.013}$	
e_d	$0.014^{+0.016}_{-0.01}$	
e_e	$0.283^{+0.064}_{-0.071}$	
Kepler-68		
P_b	$\equiv 5.3988$	days
P_c	$\equiv 9.6051$	days
P_d	$634.6^{+4.1}_{-3.7}$	days
M_b	$7.65^{+1.37}_{-1.32}$	M_{\oplus}
M_c	$2.04^{+1.72}_{-1.78}$	M_{\oplus}
$M_d \sin i$	$0.77^{+0.03}_{-0.03}$	M_{Jupiter}
e_d	$0.112^{+0.035}_{-0.034}$	

also points to high masses and density for the transiting planets of Kepler-25, consistent with previous work suggesting they may be in a low-eccentricity, periodic configuration (Migaszewski & Goździewski 2018).

We also consider the possibility that the observed long-period, eccentric giant planets are actually a pair of giant planets near a 2:1 mean motion resonance (Anglada-Escudé et al. 2010; Wittenmyer et al. 2013; Kürster et al. 2015). We perform a model comparison between a single, eccentric giant planet model and two giant planets on circular orbits for each system following Boisvert et al. (2018). Kepler-65 shows no support for a two-giant-planet model, strengthening our earlier finding of a single moderately eccentric giant planet in the system. However, the model comparisons between a single giant and a pair of giants in the Kepler-25 and Kepler-68 systems are inconclusive but suggestive of a pair of giants just outside 2:1 resonance. We therefore urge further RV monitoring of both systems to definitively rule out (or confirm) near-resonant giant planet pairs.

Kepler-65 e ($e = 0.28 \pm 0.07$) is one of the highest eccentricity giant planets discovered to date exterior to a system of compact SEASNs. The relatively high eccentricities of Kepler-65 e and Kepler-68 d ($e = 0.11 \pm 0.03$) compared to the low ($e < 0.1$) eccentricities found in most multiplanet systems suggest that the processes which generate moderate giant planet eccentricity are not necessarily barriers to maintaining coplanar multi-planet systems at short orbital periods. In fact, these relatively high eccentricities may help reconcile the broad distribution of eccentricities seen in RV-detected giant planets with the low eccentricities seen in transiting compact multis (Fig. 1). However, they still do not reach the very high eccentricities (0.7–0.9) of some long-period planets detected with RVs, as such orbits may directly destabilize inner planets.

Mustill et al. (2015) point out that giant planets with $P \lesssim 1$ year and moderate eccentricities can be produced by high eccentricity migration channels; however, this evolutionary pathway destroys any compact interior planetary system. On the other hand, Chatterjee et al. (2008) show that giant planets processed via scattering yields a broad range of eccentricities, including producing moderate eccentricity giant planets down to semi-major axes of a few tenths of an AU. We thus tentatively suggest that these systems experienced giant

planet scattering events that did not disrupt the dynamically well-separated interior planets after their formation, rather than high eccentricity migration.

Since we expect giant planets to form rapidly to allow sufficient time for runaway gas accretion before the protoplanetary disk dissipates (Lissauer 1987; Pollack et al. 1996; Lissauer et al. 2009), we note that pebble accretion theories of SEASN formation (e.g., Johansen & Lambrechts 2017; Ormel 2017) could be disfavored in systems such as these with exterior giant planets on a wide range of radii that may halt pebble inflow (Lin & Papaloizou 1986; Lambrechts et al. 2014; Morbidelli et al. 2016). However, the influence on giant planets in pebble accretion theories remains uncertain (c.f., Hasegawa & Pudritz 2011; Morbidelli & Nesvorný 2012). The discovery of giant planets exterior to compact multiplanet systems may also disfavor large-scale migration of the inner bodies, despite the near-resonance observed in Kepler-25 (Izidoro et al. 2015).

Overall, measuring the prevalence and eccentricities of giant planets exterior to compact SEASN systems puts constraints on the formation channels of the inner planets. Additional long-term monitoring of SEASN systems is needed to increase the number of detected outer companions and the number of systems with strong limits on the non-existence of giant planets. An increase in our understanding of the statistical distribution of exterior giants will provide further insight into both the giant planets’ own dynamical histories and their influence on compact SEASN systems.

We thank the Kepler and Gaia teams for years of work making these precious datasets possible. This research has made use of NASA’s Astrophysics Data System, the Exoplanet Orbit Database, and the Exoplanet Data Explorer at exoplanets.org. M.R.K. acknowledges support from the NSF Graduate Research Fellowship, grant No. DGE 1339067. L.M.W. acknowledges support from the Beatrice Watson Parrent Fellowship, the Trottier Family Foundation, and the Levy family. The authors wish to recognize and acknowledge the very significant cultural role and reverence that the summit of Maunakea has long had within the indigenous Hawaiian community. We are most fortunate to have the opportunity to conduct observations from this mountain.

Facilities: Keck (HIRES), Kepler

Software: radvel (Fulton et al. 2018)

REFERENCES

- Agol, E., & Deck, K. 2016, *ApJ*, 818, 177
- Agol, E., Steffen, J., Sari, R., & Clarkson, W. 2005, *MNRAS*, 359, 567

- Akaike, H. 1974, *IEEE Transactions on Automatic Control*, 19, 716
- Albrecht, S., Winn, J. N., Marcy, G. W., et al. 2013, *ApJ*, 771, 11
- Anglada-Escudé, G., López-Morales, M., & Chambers, J. E. 2010, *ApJ*, 709, 168
- Batygin, K., & Laughlin, G. 2015, *Proceedings of the National Academy of Science*, 112, 4214
- Becker, J. C., Vanderburg, A., Adams, F. C., Rappaport, S. A., & Schwengeler, H. M. 2015, *ApJL*, 812, L18
- Boisvert, J. H., Nelson, B. E., & Steffen, J. H. 2018, *MNRAS*, 480, 2846
- Borucki, W. J., Koch, D., Basri, G., et al. 2010, *Science*, 327, 977
- Bryan, M. L., Knutson, H. A., Fulton, B., et al. 2018, *ArXiv e-prints*, arXiv:1806.08799
- Burnham, K. P., & Anderson, D. R. 2002, *Model selection and multimodel inference: a practical information-theoretic approach* (Springer NY)
- Cabrera, J., Csizmadia, S., Lehmann, H., et al. 2014, *ApJ*, 781, 18
- Chaplin, W. J., Sanchis-Ojeda, R., Campante, T. L., et al. 2013, *ApJ*, 766, 101
- Chatterjee, S., Ford, E. B., Matsumura, S., & Rasio, F. A. 2008, *ApJ*, 686, 580
- Christiansen, J. L., Jenkins, J. M., Caldwell, D. A., et al. 2013, *KSCI*
- Coughlin, J. L., Mullally, F., Thompson, S. E., et al. 2016, *ApJS*, 224, 12
- Dawson, R. I., Johnson, J. A., Fabrycky, D. C., et al. 2014, *ApJ*, 791, 89
- Deck, K. M., & Agol, E. 2015, *ApJ*, 802, 116
- . 2016, *ApJ*, 821, 96
- Dressing, C. D., Charbonneau, D., Dumusque, X., et al. 2015, *ApJ*, 800, 135
- Fabrycky, D. C., Lissauer, J. J., Ragozzine, D., et al. 2014, *ApJ*, 790, 146
- Foreman-Mackey, D., Hogg, D. W., Lang, D., & Goodman, J. 2013, *PASP*, 125, 306
- Foreman-Mackey, D., Morton, T. D., Hogg, D. W., Agol, E., & Schölkopf, B. 2016, *AJ*, 152, 206
- Fulton, B. J., & Petigura, E. A. 2018, *AJ*, 156, 264
- Fulton, B. J., Petigura, E. A., Blunt, S., & Sinukoff, E. 2018, *PASP*, 130, 044504
- Fulton, B. J., Petigura, E. A., Howard, A. W., et al. 2017, *AJ*, 154, 109
- Gaia Collaboration, Brown, A. G. A., Vallenari, A., et al. 2018, *A&A*, 616, A1
- García, R. A., Hekker, S., Stello, D., et al. 2011, *MNRAS*, 414, L6
- Gelman, A., & Rubin, D. B. 1992, *Statistical Science*, 7, 457
- Gilliland, R. L., Marcy, G. W., Rowe, J. F., et al. 2013, *ApJ*, 766, 40
- Ginski, C., Mugrauer, M., Seeliger, M., et al. 2016, *MNRAS*, 457, 2173
- Hadden, S., & Lithwick, Y. 2014, *ApJ*, 787, 80
- . 2017, *AJ*, 154, 5
- Han, E., Wang, S. X., Wright, J. T., et al. 2014, *PASP*, 126, 827
- Hasegawa, Y., & Pudritz, R. E. 2011, *MNRAS*, 417, 1236
- Holczer, T., Mazeh, T., Nachmani, G., et al. 2016, *ApJS*, 225, 9
- Howard, A. W., Johnson, J. A., Marcy, G. W., et al. 2010, *ApJ*, 721, 1467
- Huang, C. X., Petrovich, C., & Deibert, E. 2017, *AJ*, 153, 210
- Izidoro, A., Raymond, S. N., Morbidelli, A., Hersant, F., & Pierens, A. 2015, *ApJL*, 800, L22
- Johansen, A., & Lambrechts, M. 2017, *Annual Review of Earth and Planetary Sciences*, 45, 359
- Johnson, J. A., Howard, A. W., Bowler, B. P., et al. 2010, *PASP*, 122, 701
- Kürster, M., Trifonov, T., Reffert, S., Kostogryz, N. M., & Rodler, F. 2015, *A&A*, 577, A103
- Lambrechts, M., Johansen, A., & Morbidelli, A. 2014, *A&A*, 572, A35
- Lin, D. N. C., & Papaloizou, J. 1986, *ApJ*, 309, 846
- Lissauer, J. J. 1987, *Icarus*, 69, 249
- Lissauer, J. J., Hubickyj, O., D’Angelo, G., & Bodenheimer, P. 2009, *Icarus*, 199, 338
- Lithwick, Y., Xie, J., & Wu, Y. 2012, *ApJ*, 761, 122
- Lomb, N. R. 1976, *Ap&SS*, 39, 447
- Lopez, E. D., & Fortney, J. J. 2013, *ApJ*, 776, 2
- Lopez, E. D., & Rice, K. 2018, *MNRAS*, 479, 5303
- Marcy, G. W., Butler, R. P., Vogt, S. S., et al. 2008, *Physica Scripta Volume T*, 130, 014001
- Marcy, G. W., Isaacson, H., Howard, A. W., et al. 2014, *ApJS*, 210, 20
- Mazeh, T., Nachmani, G., Holczer, T., et al. 2013, *ApJS*, 208, 16
- Migaszewski, C., & Goździewski, K. 2018, *MNRAS*, 480, 1767
- Morbidelli, A., & Nesvorný, D. 2012, *A&A*, 546, A18
- Morbidelli, A., Bitsch, B., Crida, A., et al. 2016, *Icarus*, 267, 368
- Morton, T. D., Bryson, S. T., Coughlin, J. L., et al. 2016, *ApJ*, 822, 86
- Mustill, A. J., Davies, M. B., & Johansen, A. 2015, *ApJ*, 808, 14

- Nesvorný, D., Kipping, D. M., Buchhave, L. A., et al. 2012, *Science*, 336, 1133
- Ofir, A., Xie, J.-W., Jiang, C.-F., Sari, R., & Aharonson, O. 2018, *ApJS*, 234, 9
- Ormel, C. W. 2017, in *Astrophysics and Space Science Library*, Vol. 445, *Astrophysics and Space Science Library*, ed. M. Pessah & O. Gressel, 197
- Owen, J. E., & Wu, Y. 2013, *ApJ*, 775, 105
- . 2017, *ApJ*, 847, 29
- Pál, A. 2012, *MNRAS*, 420, 1630
- Petigura, E. A., Benneke, B., Batygin, K., et al. 2018, *AJ*, 156, 89
- Pollack, J. B., Hubickyj, O., Bodenheimer, P., et al. 1996, *Icarus*, 124, 62
- Pu, B., & Lai, D. 2018, *MNRAS*, 478, 197
- Scargle, J. D. 1982, *ApJ*, 263, 835
- Sinukoff, E., Howard, A. W., Petigura, E. A., et al. 2017, *AJ*, 153, 70
- Steffen, J. H., Fabrycky, D. C., Ford, E. B., et al. 2012, *MNRAS*, 421, 2342
- Ter Braak, C. J. F. 2005, Wageningen UR, *Biometris*, 010404, 556
- Uehara, S., Kawahara, H., Masuda, K., Yamada, S., & Aizawa, M. 2016, *ApJ*, 822, 2
- Van Eylen, V., & Albrecht, S. 2015, *ApJ*, 808, 126
- Van Eylen, V., Albrecht, S., Huang, X., et al. 2019, *AJ*, 157, 61
- Wittenmyer, R. A., Wang, S., Horner, J., et al. 2013, *ApJS*, 208, 2
- Xie, J.-W., Dong, S., Zhu, Z., et al. 2016, *Proceedings of the National Academy of Science*, 113, 11431
- Zhu, W., Petrovich, C., Wu, Y., Dong, S., & Xie, J. 2018, *ApJ*, 860, 101
- Zhu, W., & Wu, Y. 2018, *AJ*, 156, 92

APPENDIX

Table 7. Kepler-25 HIRES RVs

Time	RV	σ	S-value
[BJD-2454900]	m s ⁻¹	m s ⁻¹	
467.103	-7.25	3.84	0.133
476.963	3.64	3.27	0.132
477.950	-2.84	3.17	0.134
533.942	14.53	3.65	0.127
796.949	13.33	3.42	0.131
797.952	2.34	3.67	0.130
798.949	-4.09	3.46	0.130
800.028	10.93	3.55	0.131
834.053	-0.47	3.06	0.132
834.942	-2.08	2.92	0.131
835.987	-13.09	3.24	0.132
839.050	-2.54	4.08	0.132
851.936	-15.48	3.34	0.133
852.794	-18.31	2.96	0.132
859.966	6.28	2.94	0.133
860.810	-4.88	3.10	0.133
861.103	-3.76	2.98	0.133
861.775	-0.48	3.61	0.130
862.110	2.11	3.35	0.131
862.891	-2.22	2.56	0.132
863.841	-6.79	2.96	0.130
868.853	-8.20	3.26	0.096
869.944	9.28	3.54	0.124
882.065	-5.56	4.07	0.129
887.763	-0.92	3.71	0.130
888.938	-4.86	3.29	0.128
889.798	1.53	3.60	0.128
889.805	4.00	4.06	0.129
890.756	-2.39	3.27	0.129
891.933	-0.20	3.31	0.128
892.767	3.39	3.15	0.128
894.926	17.73	3.71	0.126
896.893	16.41	3.38	0.128
898.759	4.48	3.38	0.127
906.789	15.13	3.49	0.126
908.797	20.58	3.12	0.127
910.735	7.32	3.49	0.127
914.927	15.07	3.57	0.126
1003.699	10.62	3.48	0.127
1179.873	-0.50	3.93	0.122
1180.110	4.38	3.55	0.131
1214.852	4.21	3.84	0.135
1234.930	-11.01	3.27	0.130
1239.028	-2.79	3.54	0.131
1245.944	-1.82	4.20	0.131
1247.807	-5.27	3.46	0.130
1248.840	-6.27	3.87	0.129
1252.963	15.96	3.70	0.128
1263.794	23.03	3.54	0.129
1294.822	7.34	4.06	0.127
1575.858	-12.85	3.69	0.133

Table 7 continued

Table 7 (*continued*)

Time	RV	σ	S-value
[BJD-2454900]	m s ⁻¹	m s ⁻¹	
1619.908	17.03	3.91	0.129
1946.047	-1.94	3.33	0.131
1946.900	-21.44	3.50	0.132
1966.904	-10.92	3.84	0.122
1984.002	3.68	3.92	0.127
2010.879	1.79	3.91	0.127
2280.055	14.22	3.69	0.128
2301.960	-11.52	3.73	0.133
2303.050	-20.87	3.61	0.132
2308.083	-4.48	3.87	0.125
2311.917	4.81	3.68	0.134
2318.056	-5.55	3.62	0.128
2329.923	6.56	3.85	0.133
2332.886	-0.78	4.21	0.131
2342.971	-9.59	3.98	0.130
2345.851	2.25	4.09	0.131
2696.075	-10.85	3.85	0.128
2778.791	1.93	4.21	0.117
3046.032	5.98	3.44	0.133
3427.758	2.79	3.76	0.135

Table 8 (*continued*)**Table 8.** Kepler-65 HIRES RVs

Time	RV	σ	S-value
[BJD-2454900]	m s ⁻¹	m s ⁻¹	
797.9785	-1.46	3.03	0.1330
798.9780	0.13	2.76	0.1340
800.0428	-5.06	2.92	0.1350
835.9620	-6.07	2.64	0.1300
839.0158	-13.93	3.09	0.1330
1950.0654	-13.73	3.60	0.1333
1962.0654	-7.68	3.90	0.1340
1965.0787	-5.94	3.70	0.1372
1965.7623	-7.32	3.69	0.1329
1966.9672	-4.24	3.75	0.1306
1972.9521	5.86	3.60	0.1290
1980.9310	-4.06	3.12	0.1360
1991.8251	13.12	3.14	0.1361
1993.0213	1.71	3.20	0.1349
1994.9791	5.55	3.20	0.1354
2006.9404	12.55	3.57	0.1350
2010.8677	4.34	3.69	0.1375
2012.9413	8.11	3.59	0.1290
2101.7114	1.92	3.72	0.1305
2251.0331	18.43	3.40	0.1338
2279.9614	18.66	3.43	0.1288
2298.0195	25.93	3.20	0.1312
2303.0104	31.70	3.55	0.1331
2311.0792	20.51	3.57	0.1344
2316.0349	15.53	3.36	0.1331
2322.0992	11.10	3.44	0.1356

Table 8 continued

Time	RV	σ	S-value
[BJD-2454900]	m s ⁻¹	m s ⁻¹	
2323.1172	22.54	3.18	0.1339
2329.0174	9.84	3.37	0.1350
2329.9147	5.22	3.31	0.1360
2330.7927	19.60	3.41	0.1369
2332.0814	16.24	3.29	0.1355
2332.8916	12.18	3.53	0.1355
2334.1023	8.54	3.31	0.1323
2335.9536	2.34	3.20	0.1357
2336.8389	14.48	3.22	0.1367
2340.0231	8.16	2.92	0.1361
2344.8161	8.01	3.12	0.1383
2345.9187	-9.75	3.04	0.1380
2347.0604	-14.91	3.38	0.1359
2353.9886	5.19	3.01	0.1373
2354.9137	-6.50	3.17	0.1351
2356.0186	-1.05	3.48	0.1188
2362.8601	-22.99	3.38	0.1377
2364.9807	-9.91	3.21	0.1378
2385.7684	-19.79	3.40	0.1335
2390.8331	-9.75	3.41	0.1337
2390.9402	-5.77	3.85	0.1226
2394.8182	-5.33	3.04	0.1364
2396.9131	-22.19	3.32	0.1321
2398.7801	-13.78	3.18	0.1334
2426.7046	-4.02	3.38	0.1330
2426.8396	-10.35	3.63	0.1340
2453.6800	-6.67	3.15	0.1374
2453.7663	-17.74	3.56	0.1347
2454.6923	-0.05	3.18	0.1584

Table 8 continued

Table 8 (*continued*)

Time	RV	σ	S-value
[BJD-2454900]	m s ⁻¹	m s ⁻¹	
2454.7650	-7.60	3.49	0.1357
2455.6847	-7.21	3.45	0.1352
2455.7584	-7.93	3.29	0.1346
2478.6966	-10.71	3.75	0.1214
2540.1678	21.70	3.28	0.1312
2578.1258	16.72	3.70	0.1340
2620.9898	9.11	3.28	0.1350
2662.0773	-7.37	3.14	0.1324
2669.9411	-17.18	4.17	0.1335
2680.0415	-3.02	3.59	0.1336
2684.0287	-26.03	3.77	0.1326
2697.0877	-19.14	4.43	0.1359
2772.8783	11.25	3.17	0.1352
2988.0677	-7.14	3.56	0.1332
3027.0476	2.71	3.37	0.1337

Table 9. Kepler-68 HIRES RVs

Time	RV	σ	S-value
[BJD-2454900]	m s ⁻¹	m s ⁻¹	
413.082	-6.16	1.47	0.140
419.109	-9.77	1.72	0.135
422.051	-12.09	1.26	0.138
472.983	-11.05	1.18	0.138
477.929	-9.73	1.21	0.139
481.000	-17.54	1.27	0.138
496.963	-14.63	1.52	0.140
512.923	-18.64	1.19	0.137
526.913	-16.56	1.20	0.143
531.784	-10.77	1.19	0.140
534.870	-23.21	1.21	0.144
534.876	-24.48	1.20	0.144
535.931	-19.72	1.33	0.138
536.968	-15.75	1.69	0.135
536.975	-21.13	1.76	0.131
537.940	-15.08	1.32	0.143
537.950	-14.53	1.28	0.145
538.991	-15.84	1.27	0.139
539.003	-16.08	1.39	0.141
539.924	-19.47	1.19	0.144
539.932	-21.57	1.31	0.142
540.971	-18.38	1.21	0.143
540.980	-21.99	1.24	0.141
555.810	-22.84	1.28	0.148
590.830	-18.38	1.36	0.147
772.026	17.17	1.12	0.138
772.998	14.20	1.29	0.137
773.996	18.22	1.37	0.139
796.974	21.13	1.30	0.140
797.964	23.13	1.43	0.140
798.962	16.30	1.28	0.139
822.995	21.99	1.40	0.137

*Table 9 continued***Table 9** (*continued*)

Time	RV	σ	S-value
[BJD-2454900]	m s ⁻¹	m s ⁻¹	
824.034	27.13	1.47	0.137
828.901	22.75	1.51	0.125
834.064	24.72	1.35	0.137
834.951	25.41	1.31	0.138
835.975	24.25	1.32	0.138
839.034	23.77	1.41	0.137
851.797	18.56	1.44	0.138
852.105	17.53	1.33	0.134
852.779	15.36	1.36	0.138
859.975	18.30	1.32	0.139
861.076	21.53	1.18	0.139
861.842	15.24	1.23	0.134
863.033	18.81	1.29	0.132
863.851	14.05	1.26	0.139
882.908	15.18	1.35	0.137
895.024	7.12	1.53	0.139
914.736	12.55	1.19	0.146
1177.045	-16.44	1.34	0.136
1198.094	-12.64	1.44	0.137
1198.829	-13.56	1.42	0.140
1202.008	-6.61	1.30	0.138
1214.872	-15.53	1.30	0.139
1245.875	-10.22	1.39	0.141
1248.929	-4.14	1.17	0.144
1251.061	-11.05	1.31	0.142
1253.983	-9.76	1.21	0.146
1274.827	-1.96	1.40	0.147
1445.155	17.07	1.36	0.138
1575.844	9.71	1.42	0.139
1598.070	2.62	1.36	0.138
1613.044	-2.67	1.36	0.141
1619.920	-0.83	1.27	0.143
1946.882	10.49	1.36	0.137
1992.760	7.75	1.28	0.146
1992.766	8.52	1.25	0.145
1992.772	10.66	1.26	0.145
2006.735	11.57	1.24	0.145
2006.741	14.37	1.31	0.145
2006.747	14.08	1.27	0.144
2303.075	-2.44	1.27	0.136
2303.083	-2.39	1.27	0.134
2318.103	-2.05	1.36	0.140
2333.059	-15.79	1.38	0.138
2333.066	-10.99	1.44	0.139
2721.887	14.31	1.21	0.146
2721.895	8.94	1.27	0.146
2751.902	12.20	1.40	0.146
3045.018	-22.38	1.30	0.140
3102.985	-19.95	1.39	0.144
3427.765	5.31	1.35	0.143

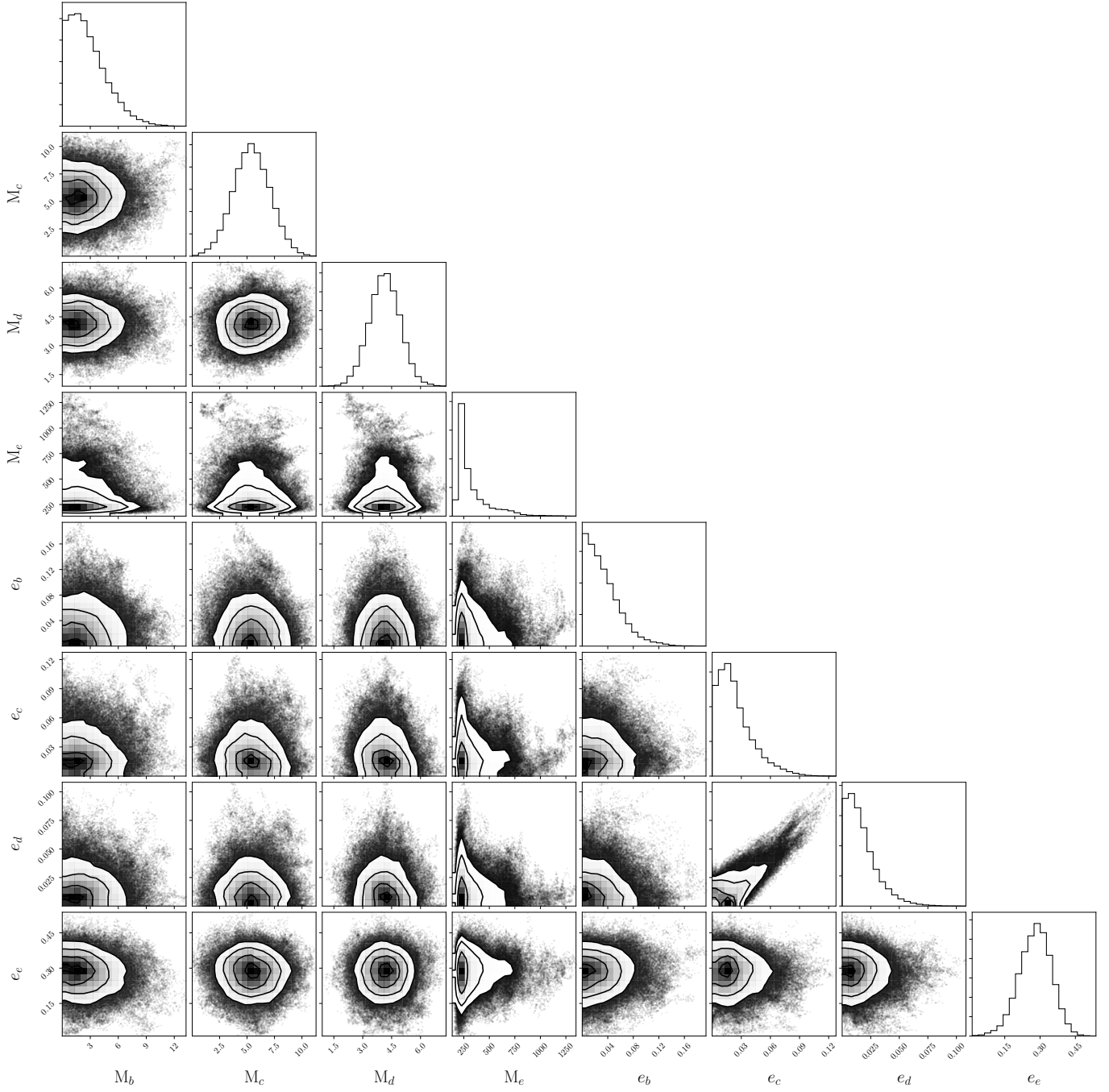


Figure 14. Mass and derived eccentricity posteriors of Kepler-65’s planets from a joint RV-*Kepler* photometry fit. A significant TTV detection by the photodynamic model, combined with the low eccentricity prior results in mass constraints weakly degenerate with eccentricity.

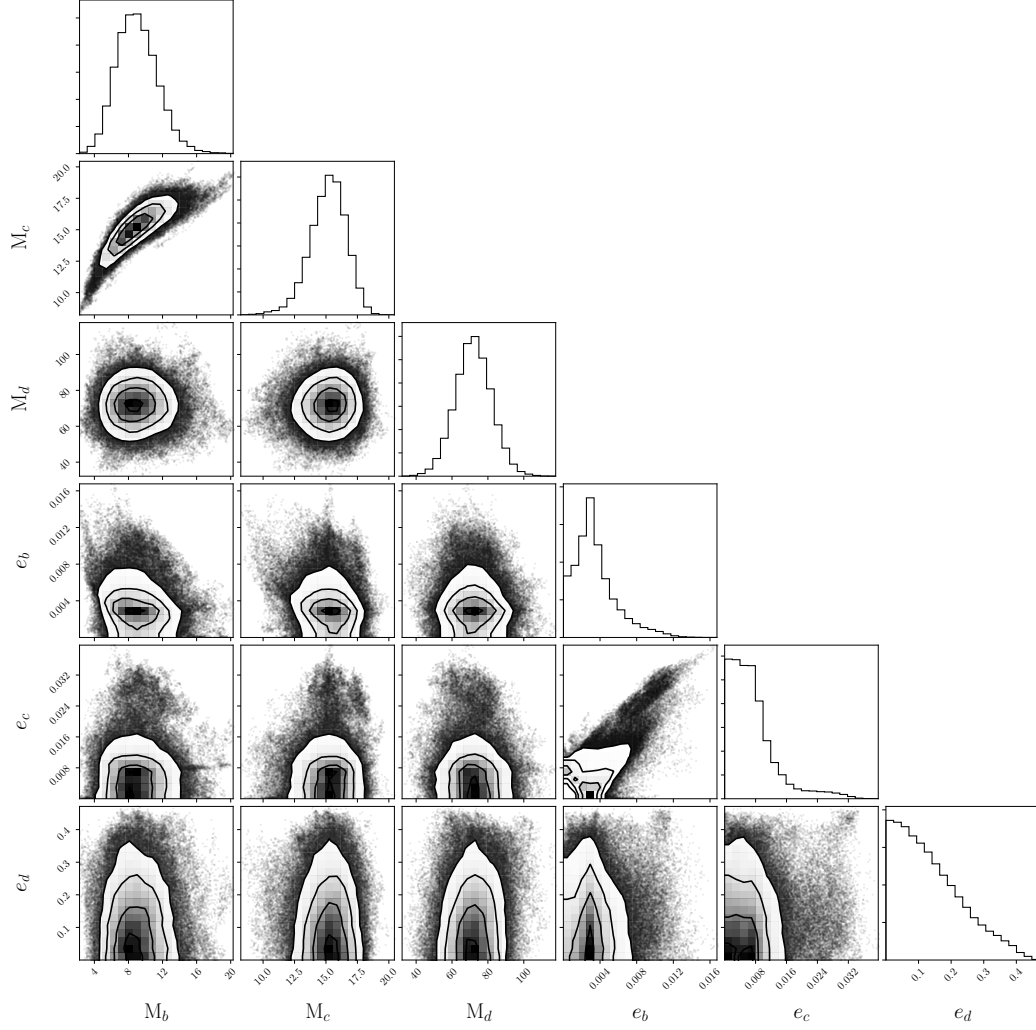


Figure 15. Mass and derived eccentricity posteriors from a joint RV-*Kepler* photometry fit of Kepler-25. A significant TTV detection by the photodynamic model, combined with the low eccentricity prior results in mass constraints weakly degenerate with eccentricity.